THE JOURNAL OF PHYSICAL CHEMISTRY B
A JOURNAL OF THE AMERICAN CHEMICAL SOCIETY

pubs.acs.org/JPCB

Article

Ligand–Ligand-Interaction-Dominated Self-Assembly of Gold Nanoparticles at the Oil/Water Interface: An Atomic-Scale Simulation

Haihong Jia,[‖] Yan-Fang Zhang,[‖] Chunlei Zhang, Min Ouyang, and Shixuan Du*

Cite This: *J. Phys. Chem. B* 2023, 127, 2258–2266

Read Online

ACCESS | Metrics & More | Article Recommendations | Supporting Information

ABSTRACT: The self-assembly of nanoparticles (NPs) into ordered superlattices is a powerful strategy to fabricate functional nanomaterials. Subtle variations in the interactions between NPs will influence the self-assembled superlattices. Using all-atom molecular dynamics simulations, we explore the self-assembly of 16 gold NPs, 4 nm in diameter, capped with ligands at the oil–water interface, and quantify the interactions between NPs at the atomic scale. We demonstrate that the interaction between capping ligands rather than that between NPs is dominant during the assembly process. For dodecanethiol (DDT)-capped Au NPs, the assembled superlattice is highly ordered in a close-packed configuration at a slow evaporation rate, while it is disordered at a fast evaporation rate. When replacing the capping ligands with stronger polarization than DDT molecules, the NPs form a robust ordered configuration at different evaporation rates due to the stronger electrostatic attraction between capping ligands from different NPs. Moreover, Au–Ag binary clusters exhibit similar assembly behavior with Au NPs. Our work uncovers the nonequilibrium nature of NP assembly at the atomic scale and would be helpful in rationally controlling NPs superlattice by changing passivating ligands, solvent evaporation rate, or both.

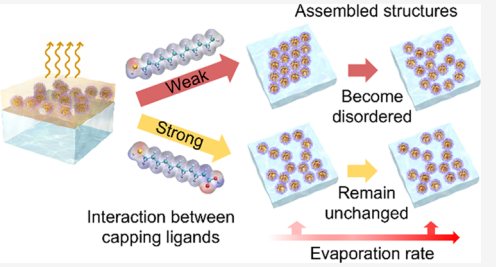

INTRODUCTION

Nanoparticles (NPs) stabilized with capping ligands have been widely used as building blocks in nanotechnology.[1,2] They organize spontaneously into ordered structures, which are necessary for high-performance nanodevices, such as optical sensors,[3] optical imaging,[4] energy storage,[5] and light emitting devices.[6] The self-assembly of NPs in solution is an important and robust "bottom-up" method for obtaining ordered, well-defined, and easily transferred nanoarchitectures with a large area and high quality.[7−15] Great experimental efforts have been devoted to delicately modulating the driving force for effectively controlling self-assembly. For example, capping ligands are tailored to tune the interaction potentials between NPs to shape the self-assembly of NPs into a distinct superlattice.[16−18] In addition, adjusting the evaporation rate of solvents, either by choice of solvent, temperature, or solvent partial pressure, achieves a kinetical control of the self-assembled superlattice.[19−21] These studies reveal that a subtle change in the environmental conditions will lead to totally different structures. Therefore, understanding the interactions that govern the self-assembly process at the atomic scale is essential for the precise control of the self-assembled structures. Nevertheless, the assembly mechanism, especially the role of the capping layer, at the atomistic level in solution has rarely been elucidated.

Experimentally characterizing the dynamic behavior of the NPs self-assembly in solution usually is limited to indirect measurement techniques, such as small-angle X-ray scattering spectroscopy,[22−24] UV–vis spectroscopy,[25,26] optical imaging strategy,[9,27] etc. It should be noted that although these techniques can detect the evolution of ensembles as a whole, they omit the interaction among individual NPs at different stages during the self-assembly process. In situ liquid cell transmission electron microscopy (LC-TEM) emerges as a powerful tool to detect the interactions between NPs and their self-assembly by directly imaging transient stages in thin liquid films at a nanoscale.[28−31] However, several challenges have hindered a straightforward interpretation of the LC-TEM experimental observations, such as the high energy of the electron beam that may cause the dissolution of metal NPs[32] and the confinement and surface effects within the liquid cells that may influence the diffusive motion of NPs.[33]

Alternatively, molecular dynamics (MD) or Monte Carlo (MC) simulations based on a coarse-grained (CG) model offer a detailed view of the key intermediate states of the NP assembly for large-scale systems.[34−38] Nevertheless, a precise description of the interactions that control the assembly of NPs

Received: November 13, 2022
Revised: January 31, 2023
Published: March 3, 2023

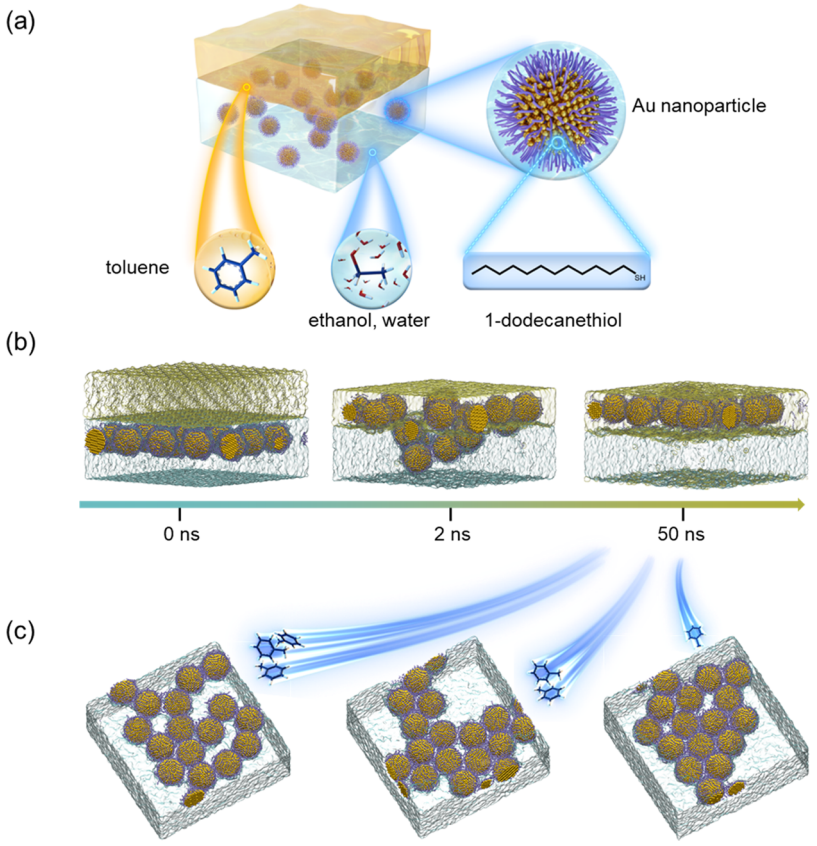

Figure 1. Configurations of 16 Au NPs before and after MD simulation at 300 K under NPT ensemble. (a) Schematic of 16 Au NPs in the solvent containing TOL molecules (oil phase) and ethanol−water mixtures (water phase). (b) Evolution of the position of Au NPs during a 50 ns simulation time. (c) Assembled NP arrays after the oil evaporation at evaporation rates of 1000, 200, and 50 ns^{-1} (from left to right).

in solutions is rare because the CG model often neglects NPs' internal structure and the sizable layer of organic ligands passivating each NP's surface. Recently, based on coarse-grained molecular dynamics (CGMD) simulation results, Zhou et al. found that bilayer-polymer-grafted nanocubes assemble into a variety of unusual architectures by changing the grafting density and miscibility, demonstrating the vital role of the capping ligands in the self-assembly process.[39] However, it is still difficult to achieve precise control over particle orientation and position in experiments due to the absent description of the self-assembly process at an atomic scale and the loss of atomic information of capping ligands. All-atom MD simulations, which are able to visualize the entire process at the atomic level, show advantages in describing intermolecular forces between NPs at the nanoscale. Furthermore, they have been used to analyze the interaction energy between two $S(CH_2)_nCOOH$-coated Au NPs during the coalescence process.[40] However, the self-assembly process of multi-NPs induced by solvent evaporation in solution has been rarely explored by all-atom MD simulations due to the complex environment of the solution and the high computational cost.

Here, using all-atom MD simulations, we investigate the self-assembly behavior of 16 spherical Au NPs with 1-dodecanethiol (DDT) molecules as capping ligands at the toluene−ethanol/water mixture interface upon the evaporation of toluene (TOL) molecules. By analyzing the interaction energies, we find that the interaction between capping ligands, especially van der Waals (vdW) interactions, dominates the assembly process. The structures obtained at various evaporation rates are characterized by the radial distribution function (RDF) in combination with the bond-orientational order parameter. The results reveal that the slower the evaporation rate, the easier it is to form a two-dimensional (2D) close-packed array of Au NPs. If we replace the ligands with mercaptoundecanoic acid (MUA) molecules with strong polarization, the MUA-capped Au NPs aggregate faster and form a roughly ordered close-packed array. The self-assembly of MUA-capped NPs is negligibly influenced by the evaporation rate because MUA-capped NPs approach very fast and hardly separate once they are in contact due to the strong interaction between MUA ligands from different NPs. The interaction energy analysis also shows that the interaction between MUA molecules dominates the formation of an ordered assembly structure. Further simulations of polar NPs (Au−Ag binary clusters) using DDT as capping ligands demonstrate that the interaction between capping ligands still plays an important role. These findings provide strategies for the self-assembly to form ordered superlattices with high structural complexity by tailoring the capping ligands of NPs and solvent evaporation rate.

METHODS

All of the all-atom MD simulations were carried out using the Gromacs-4.6.7 software package.[41] The General AMBER force field was employed to describe the intra- and intermolecular interactions of ethanol, DDT, MUA, and TOL molecules. Accordingly, partial atomic charges for the three molecules were obtained by the restrained electrostatic potential (RESP) fitting method.[42,43] The interaction between Au atoms was

https://doi.org/10.1021/acs.jpcb.2c07937
J. Phys. Chem. B 2023, 127, 2258−2266

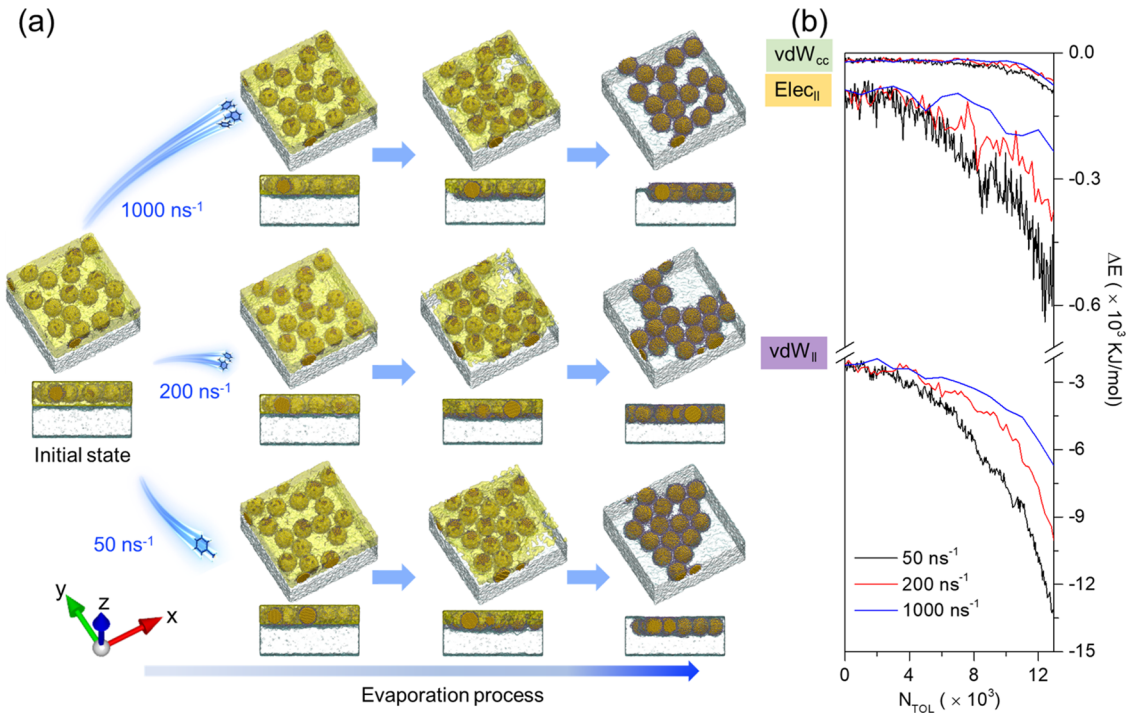

Figure 2. Snapshots of the assembled NPs arrays and the interaction energy between NPs during the evaporation process. (a) Snapshots of NP assembly during the evaporation process with the evaporation rates of 1000 ns^{-1} (top panel), 200 ns^{-1} (middle panel), and 50 ns^{-1} (bottom panel). The overhead view is captured along the left lower coordinate axis. The side view is taken along the *y*-axis. (b) Interaction energies between NPs as a function of the number of evaporated TOL molecules (N_{TOL}) during the evaporation process with evaporation rates of 1000, 200, and 50 ns^{-1}.

described by the Lennard-Jones potential.[44] For water molecules, transferable intermolecular potential with three points (TIP3P) was chosen.[45] The in-plane periodical boundary conditions were applied and two virtual walls were applied on the top and bottom of the supercell. The Berendsen thermostat and barostat were used to control the temperature and pressure, respectively.[46] A time step of 1 fs was used in all simulations. A typical 12 Å cutoff distance was used in the calculations of short electrostatic interaction as well as van der Waals interaction. Long-range electrostatic interactions were computed using the particle mesh Ewald (PME) method.

The solution comprises an ethanol−water mixture and TOL molecules forming a water/oil interface. An ethanol−water mixture is used as the aqueous phase because ethanol is a widely used inducer for the oil/water interfacial self-assembly process. Since too little inducer generally will result in a film with a low area coverage ratio and apparent gaps, while too much will cause the as-assemble film to fold,[7] the weight ratio of ethanol and water has been carefully tested. A weight ratio of 0.06 is used and is proved to be appropriate since all NPs are trapped in the oil−water interface during the self-assembly process. Sixteen spherical Au NPs with a diameter of ∼4 nm stabilized with DDT molecules were put in the ethanol−water mixture as shown in Figure 1. The DDT-capped (MUA-capped) Au NP system contains 685088 (683702) atoms, including 123872 (123410) water molecules, 3600 ethanol molecules, 16 Au NPs with 1985 atoms each, 1408 DDT (MUA) molecules, and 12960 TOL molecules. The packing density of either DDT or MUA molecules was tested to ensure that it is sufficient to prevent coalescence between the NPs. For DDT, the ligands lie on the surface of NPs. For MUA, the thiol group attaches to the surface of NPs due to the strong affinity of sulfur to gold, while the carboxy group is attracted to water due to the intermolecular hydrogen-bond interaction. A 50 ns MD simulation under NPT (1 atm, 300 K) ensemble was performed to obtain the equilibrated solution before the evaporation of the TOL molecules.

To mimic the solvent evaporation process, a quasi-equilibrium approach was employed by randomly extracting a certain number of solvent molecules from the solution at a predefined time interval, Δt (1 ns). Here, three evaporation rates, extracting 50, 200, and 1000 TOL molecules per nanosecond, were used. To achieve thermodynamic equilibrium, a 10 ns NPT simulation was performed for each system after the evaporation process.

RESULTS AND DISCUSSION

Evaporation-Induced Self-Assembly of Au NPs. Figure 1a shows the initial configuration of 16 Au NPs in the solvent containing TOL molecules (oil phase) and ethanol−water mixtures (water phase). Every Au NP is passivated by 88 DDT molecules as capping ligands, as the DDT molecules are widely used to enhance the stability of Au NPs in experiments.[47,48] Interestingly, all of the Au NPs in the water phase move into the oil phase after a 50 ns equilibration process at 300 K (Figure 1b). The interfacial accumulation of Au NPs results from the competition between the particle−oil (hydrophobic) and particle−water (hydrophilic) interactions, which can be defined as the hydrophobic/hydrophilic potential energy ratio ($R_{HO/HI} = E_{HO}/E_{HI}$).[18] Here, the E_{HO} (E_{HI}) can be obtained by calculating the interaction energy between the oil (water) and the Au NPs during the equilibration process. The $R_{HO/HI}$ increases quickly from ∼1 to ∼200 as the simulation time increases (Figure S1), indicating that the particle−oil interaction is stronger than the particle−water one. The

https://doi.org/10.1021/acs.jpcb.2c07937
J. Phys. Chem. B 2023, 127, 2258−2266

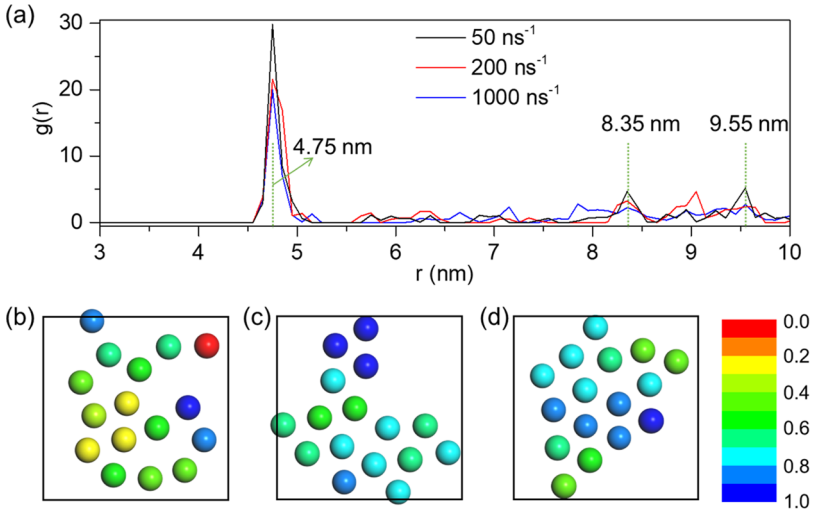

Figure 3. Structural ordering of assembled NP arrays. (a) Radial distribution function of NPs in the assembled NPs arrays. Green dashed lines indicate the first, second, and third characteristic peaks. (b–d) Hexagonal bond order parameter for each NP in Figure S6a–c, respectively. NPs are colored according to their $\psi_6^{[1]}$ values.

stronger particle–oil interaction is attributed to the strong hydrophobicity of the DDT ligands.

The interaction between solvents and the molecular structures of solvents can affect the self-assembly process because both of them dominate the evaporation rate of solvents. Evaporation-induced self-assembly of NPs at the liquid–air or liquid–liquid interface has been observed in experiments.[7,9,20,24] Moreover, different nanocrystal superstructures have been obtained experimentally by tuning the evaporation rate using different solvents.[20] Here, to simulate how different solvents affect the self-assembly process, three different evaporation rates were chosen to mimic the evaporation of different solvents. The evaporation in a simulation was realized by directly extracting a certain number of TOL molecules from the solution at a particular time interval until no TOL molecules were left. Three evaporation rates, extracting 1000 (fast), 200 (medium), and 50 (slow) TOL molecules per nanosecond, have been considered to understand its role in the NP self-assembling process. The final assembled configurations at the three evaporation rates are presented in Figure 1c. The NPs exhibit a highly ordered configuration at a low evaporation rate of 50 ns^{-1}.

To provide a direct observation of the self-assembly of Au NPs, we show snapshots of the evaporation process with evaporation rates of 1000, 200, and 50 ns^{-1} in Figure 2a. It is found that Au NPs assemble gradually at the oil–water interface as the solvent molecules evaporate. Further analysis of the average nearest neighbor number (NN) of an NP (Figure S2) shows that Au NPs under an evaporation rate of 1000 ns^{-1} are apparently looser compared with those under evaporation rates of 200 and 50 ns^{-1} after evaporating half of the TOL molecules.

Interaction Energy between NPs During the Evaporation Process. To explore the underlying mechanism and give a quantitative description of the key interactions at the nanoscale, we first analyze the evolution of the interaction energy among all of the NPs during the assembly process (Figures 2b and S3). The interaction energy is composed of the vdW interaction energy between Au cores (vdW_{cc}) and that between ligands (vdW_{ll}) and the electrostatic interaction energy between ligands ($Elec_{ll}$). We find that the interaction energies among all NPs decrease more slowly at a slower evaporation rate, suggesting that NPs approach each other more slowly under these conditions. Therefore, the NPs have enough time to achieve the thermodynamically favored configuration, i.e., a close-packed configuration, during the assembly process. When the assembly process stops, the interaction energy among all NPs at an evaporation rate of 50 ns^{-1} is the lowest (Figure 2b), producing the close-packed configuration in the bottom right panel of Figure 2a. In addition, it is the interaction between the ligands, especially the vdW interaction, that dominates the whole evaporation process. We notice that the variation of ligand species and density results in different superlattice patterns in experiments.[32,49,50] These experimental observations imply that the interaction between ligands dominates the self-assembly process, which is consistent with our simulation results. To further validate the key role of the interaction between ligands, we change the Au core to Au–Ag binary clusters. It is found that the interaction between the ligands is also dominant in this case during the self-assembly process (Figure S4), suggesting that the NPs' assembly behavior is mainly controlled by the interaction between capping ligands.

The mean square displacement (MSD) of the NPs' mass center is calculated to evaluate the mobility of NPs as follows

$$\mathrm{MSD} = \langle |r_i(t) - r_i(0)|^2 \rangle \quad (1)$$

where $r_i(t)$ denotes the mass center position of the ith NP at time t. Figure S5 clearly depicts that the mobility of NPs increases as the evaporation rate increases. The higher mobility of NPs at a faster evaporation rate further suggests that NPs do not have enough time to achieve the thermodynamically favored highly ordered configuration.

Structural Information of Assembled Configurations. We stop the assembly process after all oil molecules have been evaporated. Then, the whole system is fully relaxed to check whether the configuration changes. The relaxed configurations (Figure S6) of the three NP arrays in Figure 1c show negligible changes, suggesting that the assembly of NPs mainly occurs at the nonequilibrium solvent evaporation stage. The buckling of the mass center of NPs is less than 1 nm on the z-axis (Figure S7), indicating that the NPs form a 2D array.

https://doi.org/10.1021/acs.jpcb.2c07937
J. Phys. Chem. B 2023, 127, 2258–2266

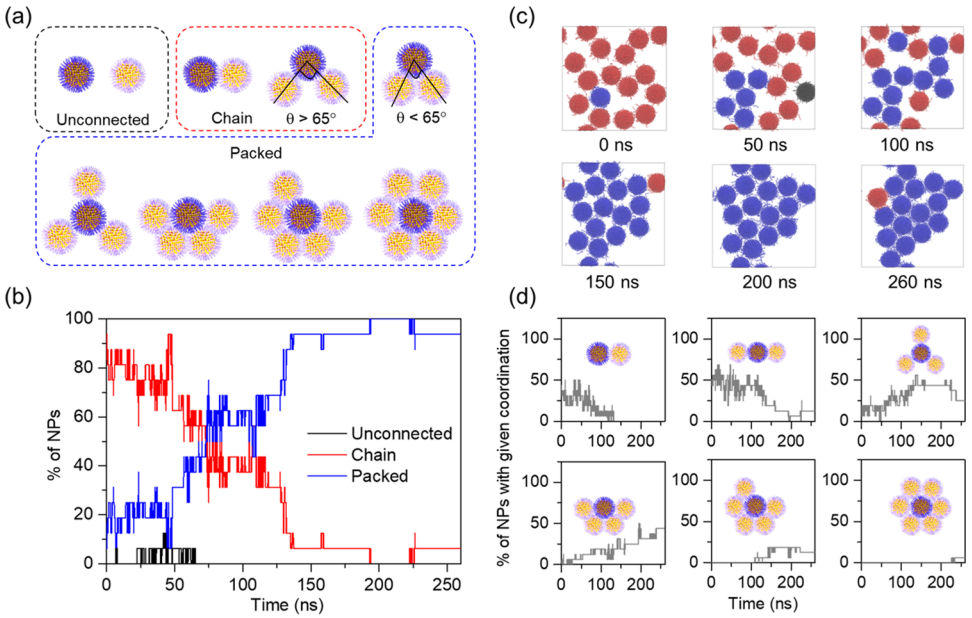

Figure 4. Evolution of NPs' configurations during the assembly at an evaporation rate of 50 ns^{-1}. (a) Schematics of the definition of the NP's configuration. (b) Distribution of NPs with unconnected (black curve), chain-like (red curve), and packed (blue curve) configurations over the assembly process. (c) Snapshots of NPs at different simulation times. NPs with packed configurations are in blue, while those with chain configurations are in red. (d) Distribution of NPs with different numbers of the nearest neighbors ranging from 1 to 6 neighbors as a function of time.

To quantitatively characterize the structures of the 2D NP arrays, we plot the in-plane (x−y plane) RDFs of the mass center of NPs, $g(r)$, (Figure 3a). For the three NP arrays formed at different evaporation rates, the first peaks of RDFs are located at around 4.75 nm. The intensity increases as the evaporation rate decreases, implying that the local order of the assembled NP arrays increases as the evaporation rate decreases. For the NP array formed at the evaporation rate of 50 ns^{-1}, the second and third RDF peaks are around 8.35 and 9.55 nm, which are approximately $\sqrt{3}$ and twice the position of the first peak. It means that the NP array formed at the evaporation rate of 50 ns^{-1} is a close-packed structure. For the NP array formed at the evaporation rate of 200 ns^{-1}, the second RDF peak is also located around 8.35 nm, while the intensity decreases compared with that of 50 ns^{-1}. Additionally, the third peak (around 9.05 nm) is less than twice that of the position of the first peak. Thus, the NP array formed at the evaporation rate of 200 ns^{-1} is less ordered than that formed at 50 ns^{-1}. For the NP array formed at the evaporation rate of 1000 ns^{-1}, the second and third RDF peaks are rather small and broad, indicating that the structure is the least ordered compared with those obtained at slower evaporation rates.

To further explore the in-plane packing geometry, the bond-orientational order parameter,[51] $\psi_6^{[1]}$, for each NP, is calculated via the following equation

$$\psi_6^{[1]} = \left| \frac{1}{M} \sum_{m=1}^{M} \exp(6i\Phi_m) \right| \quad (2)$$

where M is the number of the nearest neighbors and Φ_m is the angle between the vector from the center particle to the mth nearest neighboring particle and an arbitrary axis. $\psi_6^{[1]} = 1$ means a perfect hexagonal packing, while the limit $\psi_6^{[1]} \to 0$ corresponds to a random arrangement. The relaxed NPs are colored based on their $\psi_6^{[1]}$ values (Figure 3b−d). As shown in Figure 3b, most of the NPs are randomly distributed with $\psi_6^{[1]}$ values less than 0.5 at an evaporation rate of 1000 ns^{-1}. Figure 3c,d shows that 62.5% of NPs are characterized by a hexagonal bond order parameter, which exceeds 0.7, demonstrating that those NPs form highly ordered hexagonal-packed local structures at slower evaporation rates. Combined with the RDF results, we conclude that the slower the evaporation rate, the better the close-packed quality of the NP array.

Dynamics of NPs in the Self-Assembly Process. The NPs' configuration in each frame can be classified into three different types, unconnected, chain-like, and packed, based on the ambient environment. The configuration is defined as unconnected when the distance between the neighboring NPs is larger than 5.5 nm according to the RDF results. The chain-like configuration refers to the NP with one neighbor or two neighbors in which the angle determined by the three particles is larger than 65°. The remaining particles are then classified as packed. The definition of different NPs' configurations is shown in Figure 4a.

Figure 4b gives the NPs' configuration distribution during the assembly process with an evaporation rate of 50 ns^{-1}. Majority of the particles (93.8%) are in chain-like configurations and 6.2% are in packed configurations at the initial stage. After all solvent molecules are evaporated, only 6.2% particles are in chain-like configuration, while 93.8% are in packed configuration. The roughly inverse correlation between the chain-like and packed configuration means that the packed one is formed by the already "semi-ordered" NPs in the chain configuration. In Figure 4c, we provide representative snapshots of NPs at 0, 50, 100, 150, 200, and 260 ns. The NPs are colored based on the configuration types. The representative images clearly show that NPs adjust their positions from a low-density arrangement of chain-like configurations (red spots) to a 2D close-packed configuration (blue spots).

To better elucidate the evolution of NPs' position, we track the distribution of NPs with different numbers of neighbors as a function of simulation time, as shown in Figure 4d. In the

https://doi.org/10.1021/acs.jpcb.2c07937
J. Phys. Chem. B 2023, 127, 2258−2266

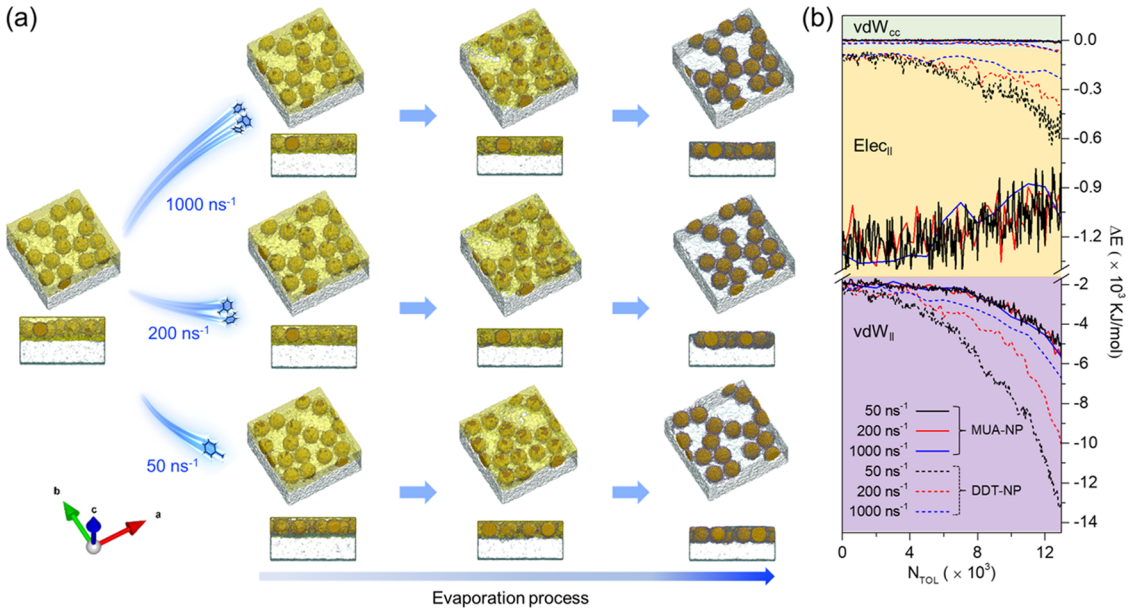

Figure 5. Snapshots of the assembled MUA-capped NPs arrays and the interaction energy between NPs during the evaporation process. (a) Snapshots of MUA-capped NP assembly during the evaporation process with the evaporation rates of 1000 ns^{-1} (top panel), 200 ns^{-1} (middle panel), and 50 ns^{-1} (bottom panel). The overhead and side views are captured along the left lower coordinate axis and along the *y*-axis. (b) Interaction energies between MUA-capped NPs as a function of the number of evaporated TOL molecules during the evaporation process with the evaporation rates of 1000, 200, and 50 ns^{-1}. The evolution of the corresponding interaction energies between DDT-capped NPs is also given by dash lines for comparison.

first 100 ns, the percentages of particles neighboring with one and two NPs decrease gradually, while those with three and four neighbors increase, which means that NPs prefer a close-packed configuration to lower the system energy. However, it takes more time for NPs to attract one more neighbor when the coordination number reaches 4. It is mainly because NPs with more neighbors are further limited to approach the surrounding NPs. Therefore, only a few NPs become hexagonally close-packed to reach an optimal coordination number of 6. For the evaporation rates of 200 or 1000 ns^{-1}, no NP has six neighbors because NPs contact with their neighbors quickly, which limits their motion and leads to the NPs trapped in a nonideal coordination environment (Figures S8 and S9).

Tuning Self-Assembled Structure by Changing Capping Ligands. To further understand the role of ligands in NPs' self-assembly process, we change the capping ligand with MUA molecules, which possess stronger intermolecular interaction than DDT molecules due to the intermolecular hydrogen bonds, which is stronger than the vdW interaction between alkyl chains in DDT (Figure S10). Figure 5 presents the snapshots and the corresponding interaction energies (vdW_{cc}, vdW_{ll}, and $Elec_{ll}$) as a function of the number of evaporated TOL molecules under three evaporation rates (50, 200, and 1000 ns^{-1}). It is observed that the MUA-capped NP array formed at the evaporation rates of 200 and 1000 ns^{-1} are almost identical (Figures 5a and S11). The slight change in the MUA-capped NP array formed at the evaporation rate of 50 ns^{-1} means that it fails to form a highly ordered hexagonal-packed local structure, which is different from the DDT-capped NPs. The interaction energies in Figure 5b also reveal that the evaporation rates have a negligible effect on the self-assembly of MUA-capped NPs, which is obviously different from the self-assembly processes of DDT-capped NPs under the same evaporation rates. The difference is induced by the quick approach of the MUA-capped NPs due to a stronger $Elec_{ll}$ in the evaporation process (Figure 5b). The stronger $Elec_{ll}$ between the MUA ligands is validated by plotting molecular electrostatic potential maps (Figure S12). Given that thiol groups of DDT molecules attach to the surface of NPs, the outer electrophilic $-(CH_2)_{11}CH_3$ groups of DDT molecules with a positive electrostatic potential (blue ellipse in Figure S12a) make neighboring NPs repel each other when they approach. Compared to DDT, the outer carboxyl of MUA has strong nucleophilic oxygen atoms (red circles in Figure S12b) and strong electrophilic hydrogen atoms (blue circle in Figure S12b), which lead to the formation of strong hydrogen bonds between two MUA molecules from neighboring NPs (Figure S10). Therefore, the coexistence of electrophilic and nucleophilic groups in MUA molecules leads to a strong electrostatic attraction between the MUA capping layers from different NPs. The strong interaction between the MUA ligands makes it difficult for the MUA-capped NPs to separate once they approach each other. Subsequently, to intuitively compare the difference in the self-assemblies of the MUA- and DDT-capped NPs, we analyze the RDFs of the MUA- and DDT-capped NPs at different evaporation times (Figure S13). The results show that MUA-capped NPs form a roughly ordered configuration very fast during solvent evaporation. While the self-assembly of DDT-capped NPs is dramatically affected by solvent evaporation since the first and second RDF peaks merge together in the last 3 ns in the solvent evaporation process.

Furthermore, the structural order of the final MUA-capped NPs array is compared with that of the DDT-capped NP array by calculating the RDFs of these NPs arrays (Figure S14). We find that the local structure of the MUA-capped NP array is less ordered than that of the DDT-capped NP array. Additionally, the first peak of the MUA-capped NP arrays shifts to a distance that is 0.1 nm longer than that of the DDT-

https://doi.org/10.1021/acs.jpcb.2c07937
J. Phys. Chem. B 2023, 127, 2258−2266

capped NP array. The 0.1 nm shift suggests that there may be a layer of water in the regions between MUA-capped NP pairs due to the high affinity of water molecules to the MUA molecules. The earlier appearance of a nonzero RDF value of water molecules for MUA-capped NPs and the magnified views of the regions between two neighboring NPs further prove that the water molecules only exist between MUA-capped neighboring NPs (Figure S15).

In the following, we discuss the influence of the thermodynamic and kinetic factors on the self-assembly and packed structures of NPs to reveal the microscopic mechanism of self-assembly. The one-order larger contribution from vdW_{II} to the interaction between NPs indicates that the interaction between capping ligands rather than that between Au cores (or Au/Ag subclusters) is the main factor in NPs' self-assembly. It demonstrates that the diversity of the assembled structures can be enriched experimentally by changing the types[18] and the density of capping ligands,[17] as well as the mixture of different types of capping ligands and so on. Therefore, next-generation colloidal semiconductor nanocrystals featuring enhanced optoelectronic properties are expected to be obtained by the rational engineering of the capping ligands.[52] We also find that the solvent evaporation rate influences the configuration of the 2D NPs array formed at the oil−water interface when the interaction between ligands is relatively weak, which has been observed in experiments.[20,21] For ligands with strong electrostatic attraction, it facilitates a quick pre-aggregation of NPs; however, it prevents the formation of highly ordered self-assembly superlattices. The MUA ligands used here have a relatively stronger electrostatic interaction than DDT ligands, which form a roughly ordered configuration faster during evaporation.

CONCLUSIONS

The self-assembly of DDT- and MUA-capped Au NPs at the oil−water interface induced by solvent evaporation has been thoroughly explored using the all-atom MD simulation method. We quantify the interaction between NPs during the self-assembly process and find that the interaction between capping ligands rather than that between Au cores is dominant. For DDT ligands with relatively weak intermolecular interaction, the NPs' self-assembly process has been regulated by the evaporation rate. A slow evaporation rate is beneficial to the formation of a highly ordered 2D NP array, since the slower evaporation rate gives NPs more time to transform chain-like configurations into a packed configuration. Noteworthy, when we replace DDT ligands with MUA ligands with a relatively strong intermolecular interaction, the self-assembly process is negligibly influenced by the evaporation rate. MUA-capped NPs form a roughly ordered configuration fast during the self-assembly process compared with DDT-capped NPs. These findings provide atomic-level insight into NP self-assembly and offer engineering strategies for NP architectures.

ASSOCIATED CONTENT

Supporting Information

The Supporting Information is available free of charge at https://pubs.acs.org/doi/10.1021/acs.jpcb.2c07937.

Hydrophobic/hydrophilic potential energy ratio for Au NPs during the equilibration process; nearest neighbor number, energy evolution, MSD, and dynamic behavior of DDT-capped Au NPs during the evaporation processes under different evaporation rates; the snapshots and density distribution profiles of equilibrated DDT-capped Au NP arrays after the evaporation; the interaction energy between DDT-capped Au−Ag NPs during the evaporation process; the configurations of MUA-capped Au NPs under different evaporation rates; the binding energies of the DDT dimer and MUA dimer; electrostatic potential maps of DDT and MUA molecules; RDFs of the MUA- and DDT-capped NPs at different evaporation times; RDFs of NPs in the assembled Au NP arrays; the binding energies, RDFs, and configurations of DDT−water and MUA−water (PDF)

AUTHOR INFORMATION

Corresponding Author

Shixuan Du − *Institute of Physics and University of Chinese Academy of Sciences, Chinese Academy of Sciences, Beijing 100190, China; Songshan Lake Materials Laboratory, Dongguan, Guangdong 523808, China;* orcid.org/0000-0001-9323-1307; Email: sxdu@iphy.ac.cn

Authors

Haihong Jia − *Institute of Physics and University of Chinese Academy of Sciences, Chinese Academy of Sciences, Beijing 100190, China*

Yan-Fang Zhang − *Institute of Physics and University of Chinese Academy of Sciences, Chinese Academy of Sciences, Beijing 100190, China*

Chunlei Zhang − *Institute of Physics and University of Chinese Academy of Sciences, Chinese Academy of Sciences, Beijing 100190, China*

Min Ouyang − *Department of Physics and Center for Nanophysics and Advanced Materials, University of Maryland, College Park, Maryland 20742, United States;* orcid.org/0000-0002-1721-1571

Complete contact information is available at: https://pubs.acs.org/10.1021/acs.jpcb.2c07937

Author Contributions

[‖]H.J. and Y.-F.Z. contributed equally to this work. S.D. conceived the research project. H.J. performed the MD simulations and data analysis. H.J. wrote the initial manuscript. All authors participated in discussing and editing the manuscript.

Notes

The authors declare no competing financial interest.

ACKNOWLEDGMENTS

The authors acknowledge financial support from the National Natural Science Foundation of China (Nos. 61888102 and 52102193), the Strategic Priority Research Program of the Chinese Academy of Sciences (No. XDB30000000), K.C. Wong Education Foundation, and the Fundamental Research Funds for the Central Universities. MD simulations were carried out on TianHe-1A at the National Supercomputer Center in Tianjin.

REFERENCES

(1) Lee, M. S.; Yee, D. W.; Ye, M.; Macfarlane, R. J. Nanoparticle Assembly as a Materials Development Tool. *J. Am. Chem. Soc.* **2022**, *144*, 3330−3346.

(2) Deng, K. R.; Luo, Z. S.; Tan, L.; Quan, Z. W. Self-Assembly of Anisotropic Nanoparticles into Functional Superstructures. *Chem. Soc. Rev.* **2020**, *49*, 6002−6038.
(3) Xavier, J.; Vincent, S.; Meder, F.; Vollmer, F. Advances in Optoplasmonic Sensors—Combining Optical Nano/Microcavities and Photonic Crystals with Plasmonic Nanostructures and Nanoparticles. *Nanophotonics* **2018**, *7*, 1−38.
(4) Liu, Q.; Zhang, Y. X.; Peng, C. S.; Yang, T. S.; Joubert, L. M.; Chu, S. Single Upconversion Nanoparticle Imaging at Sub-10 W cm−2 Irradiance. *Nat. Photonics* **2018**, *12*, 548−553.
(5) Pomerantseva, E.; Bonaccorso, F.; Feng, X.; Cui, Y.; Gogotsi, Y. Energy Storage: The Future Enabled by Nanomaterials. *Science* **2019**, *366*, No. eaan8285.
(6) Wang, T.; Zhuang, J.; Lynch, J.; Chen, O.; Wang, Z.; Wang, X.; LaMontagne, D.; Wu, H.; Wang, Z.; Cao, Y. C. Self-Assembled Colloidal Superparticles from Nanorods. *Science* **2012**, *338*, 358.
(7) Hu, L.; Chen, M.; Fang, X.; Wu, L. Oil−Water Interfacial Self-Assembly: A Novel Strategy for Nanofilm and Nanodevice Fabrication. *Chem. Soc. Rev.* **2012**, *41*, 1350−1362.
(8) Schulz, F.; Pavelka, O.; Lehmkühler, F.; Westermeier, F.; Okamura, Y.; Mueller, N. S.; Reich, S.; Lange, H. Structural Order in Plasmonic Superlattices. *Nat. Commun.* **2020**, *11*, No. 3821.
(9) Bigioni, T. P.; Lin, X.-M.; Nguyen, T. T.; Corwin, E. I.; Witten, T. A.; Jaeger, H. M. Kinetically Driven Self Assembly of Highly Ordered Nanoparticle Monolayers. *Nat. Mater.* **2006**, *5*, 265−270.
(10) Dong, A.; Chen, J.; Vora, P. M.; Kikkawa, J. M.; Murray, C. B. Binary Nanocrystal Superlattice Membranes Self-Assembled at the Liquid−Air Interface. *Nature* **2010**, *466*, 474−477.
(11) Zargartalebi, H.; Hejazi, S. H.; Sanati-Nezhad, A. Self-Assembly of Highly Ordered Micro- and Nanoparticle Deposits. *Nat. Commun.* **2022**, *13*, No. 3085.
(12) Bian, T.; Gardin, A.; Gemen, J.; Houben, L.; Perego, C.; Lee, B.; Elad, N.; Chu, Z.; Pavan, G. M.; Klajn, R. Electrostatic Co-Assembly of Nanoparticles with Oppositely Charged Small Molecules into Static and Dynamic Superstructures. *Nat. Chem.* **2021**, *13*, 940−949.
(13) Wang, D.; Dasgupta, T.; van der Wee, E. B.; Zanaga, D.; Altantzis, T.; Wu, Y.; Coli, G. M.; Murray, C. B.; Bals, S.; Dijkstra, M.; van Blaaderen, A. Binary Icosahedral Clusters of Hard Spheres in Spherical Confinement. *Nat. Phys.* **2021**, *17*, 128−134.
(14) Girard, M.; Wang, S.; Du, J. S.; Das, A.; Huang, Z.; Dravid, V. P.; Lee, B.; Mirkin, C. A.; Olvera de la Cruz, M. Particle Analogs of Electrons in Colloidal Crystals. *Science* **2019**, *364*, 1174−1178.
(15) Nagaoka, Y.; Zhu, H.; Eggert, D.; Chen, O. Single-Component Quasicrystalline Nanocrystal Superlattices through Flexible Polygon Tiling Rule. *Science* **2018**, *362*, 1396−1400.
(16) Zhu, H.; Fan, Z.; Yu, L.; Wilson, M. A.; Nagaoka, Y.; Eggert, D.; Cao, C.; Liu, Y.; Wei, Z.; Wang, X.; He, J.; Zhao, J.; Li, R.; Wang, Z.; Grünwald, M.; Chen, O. Controlling Nanoparticle Orientations in the Self-Assembly of Patchy Quantum Dot-Gold Heterostructural Nanocrystals. *J. Am. Chem. Soc.* **2019**, *141*, 6013−6021.
(17) Kim, D.; Bae, W. K.; Kim, S. H.; Lee, D. C. Depletion-Mediated Interfacial Assembly of Semiconductor Nanorods. *Nano Lett.* **2019**, *19*, 963−970.
(18) Lee, Y. H.; Shi, W.; Lee, H. K.; Jiang, R.; Phang, I. Y.; Cui, Y.; Isa, L.; Yang, Y.; Wang, J.; Li, S.; Ling, X. Y. Nanoscale Surface Chemistry Directs the Tunable Assembly of Silver Octahedra into Three Two-Dimensional Plasmonic Superlattices. *Nat. Commun.* **2015**, *6*, No. 6990.
(19) Nagaoka, Y.; Tan, R.; Li, R.; Zhu, H.; Eggert, D.; Wu, Y. A.; Liu, Y.; Wang, Z.; Chen, O. Superstructures Generated from Truncated Tetrahedral Quantum Dots. *Nature* **2018**, *561*, 378−382.
(20) Momper, R.; Zhang, H.; Chen, S.; Halim, H.; Johannes, E.; Yordanov, S.; Braga, D.; Blülle, B.; Doblas, D.; Kraus, T.; Bonn, M.; Wang, H. I.; Riedinger, A. Kinetic Control over Self-Assembly of Semiconductor Nanoplatelets. *Nano Lett.* **2020**, *20*, 4102−4110.
(21) Josten, E.; Wetterskog, E.; Glavic, A.; Boesecke, P.; Feoktystov, A.; Brauweiler-Reuters, E.; Rucker, U.; Salazar-Alvarez, G.; Bruckel, T.; Bergstrom, L. Superlattice Growth and Rearrangement During Evaporation-Induced Nanoparticle Self-Assembly. *Sci. Rep.* **2017**, *7*, No. 2802.
(22) Weidman, M. C.; Smilgies, D.-M.; Tisdale, W. A. Kinetics of the Self-Assembly of Nanocrystal Superlattices Measured by Real-Time in Situ X-Ray scattering. *Nat. Mater.* **2016**, *15*, 775−781.
(23) Jiang, Z.; Lee, B. Recent Advances in Small Angle X-Ray Scattering for Superlattice Study. *Appl. Phys. Rev.* **2021**, *8*, No. 011305.
(24) Deng, K.; Luo, Z.; Tan, L.; Quan, Z. Self-Assembly of Anisotropic Nanoparticles into Functional Superstructures. *Chem. Soc. Rev.* **2020**, *49*, 6002−6038.
(25) Kundu, P. K.; Samanta, D.; Leizrowice, R.; Margulis, B.; Zhao, H.; Börner, M.; Udayabhaskararao, T.; Manna, D.; Klajn, R. Light-Controlled Self-Assembly of Non-Photoresponsive Nanoparticles. *Nat. Chem.* **2015**, *7*, 646−652.
(26) Chen, Y.; Wang, Z.; He, Y.; Yoon, Y. J.; Jung, J.; Zhang, G.; Lin, Z. Light-Enabled Reversible Self-Assembly and Tunable Optical Properties of Stable Hairy Nanoparticles. *Proc. Natl. Acad. Sci. U.S.A.* **2018**, *115*, No. E1391.
(27) Mudanyali, O.; McLeod, E.; Luo, W.; Greenbaum, A.; Coskun, A. F.; Hennequin, Y.; Allier, C. P.; Ozcan, A. Wide-Field Optical Detection of Nanoparticles Using on-Chip Microscopy and Self-Assembled Nanolenses. *Nat. Photonics* **2013**, *7*, 247−254.
(28) Ross, F. M. Opportunities and Challenges in Liquid Cell Electron Microscopy. *Science* **2015**, *350*, No. aaa9886.
(29) Lee, W. C.; Kim, B. H.; Choi, S.; Takeuchi, S.; Park, J. Liquid Cell Electron Microscopy of Nanoparticle Self-Assembly Driven by Solvent Drying. *J. Phys. Chem. Lett.* **2017**, *8*, 647−654.
(30) Sutter, P.; Sutter, E. Real-Time Electron Microscopy of Nanocrystal Synthesis, Transformations, and Self-Assembly in Solution. *Acc. Chem. Res.* **2021**, *54*, 11−21.
(31) Tan, S. F.; Chee, S. W.; Lin, G.; Mirsaidov, U. Direct Observation of Interactions between Nanoparticles and Nanoparticle Self-Assembly in Solution. *Acc. Chem. Res.* **2017**, *50*, 1303−1312.
(32) Bhattarai, N.; Woodall, D. L.; Boercker, J. E.; Tischler, J. G.; Brintlinger, T. H. Controlling Dissolution of Pbte Nanoparticles in Organic Solvents During Liquid Cell Transmission Electron Microscopy. *Nanoscale* **2019**, *11*, 14573−14580.
(33) Chee, S. W.; Baraissov, Z.; Loh, N. D.; Matsudaira, P. T.; Mirsaidov, U. Desorption-Mediated Motion of Nanoparticles at the Liquid−Solid Interface. *J. Phys. Chem. C* **2016**, *120*, 20462−20470.
(34) Cheng, S.; Grest, G. S. Dispersing Nanoparticles in a Polymer Film Via Solvent Evaporation. *ACS Macro Lett.* **2016**, *5*, 694−698.
(35) Katiyar, P.; Singh, J. K. Evaporation Induced Self-Assembly of Different Shapes and Sizes of Nanoparticles: A Molecular Dynamics Study. *J. Chem. Phys.* **2019**, *150*, No. 044708.
(36) Cheng, S.; Grest, G. S. Molecular Dynamics Simulations of Evaporation-Induced Nanoparticle Assembly. *J. Chem. Phys.* **2013**, *138*, No. 064701.
(37) Ku, J.; Aruguete, D. M.; Alivisatos, A. P.; Geissler, P. L. Self-Assembly of Magnetic Nanoparticles in Evaporating Solution. *J. Am. Chem. Soc.* **2011**, *133*, 838−848.
(38) Rabani, E.; Reichman, D. R.; Geissler, P. L.; Brus, L. E. Drying-Mediated Self-Assembly of Nanoparticles. *Nature* **2003**, *426*, 271−274.
(39) Zhou, Y.; Tang, T.-Y.; Lee, B. H.-j.; Arya, G. Tunable Orientation and Assembly of Polymer-Grafted Nanocubes at Fluid−Fluid Interfaces. *ACS Nano* **2022**, *16*, 7457−7470.
(40) Guo, P.; Gao, Y. Coalescence of Au Nanoparticles without Ligand Detachment. *Phys. Rev. Lett.* **2020**, *124*, No. 066101.
(41) Hess, B.; Kutzner, C.; van der Spoel, D.; Lindahl, E. Gromacs 4: Algorithms for Highly Efficient, Load-Balanced, and Scalable Molecular Simulation. *J. Chem. Theory Comput.* **2008**, *4*, 435−447.
(42) Bayly, C. I.; Cieplak, P.; Cornell, W.; Kollman, P. A. A Well-Behaved Electrostatic Potential Based Method Using Charge Restraints for Deriving Atomic Charges: The Resp Model. *J. Phys. Chem. A* **1993**, *97*, 10269−10280.

(43) Fox, T.; Kollman, P. A. Application of the Resp Methodology in the Parametrization of Organic Solvents. *J. Phys. Chem. B* **1998**, *102*, 8070−8079.
(44) Heinz, H.; Vaia, R. A.; Farmer, B. L.; Naik, R. R. Accurate Simulation of Surfaces and Interfaces of Face-Centered Cubic Metals Using 12-6 and 9-6 Lennard-Jones Potentials. *J. Phys. Chem. C* **2008**, *112*, 17281−17290.
(45) Jorgensen, W. L.; Chandrasekhar, J.; Madura, J. D.; Impey, R. W.; Klein, M. L. Comparison of Simple Potential Functions for Simulating Liquid Water. *J. Chem. Phys.* **1983**, *79*, 926−935.
(46) Berendsen, H. J. C.; Postma, J. P. M.; van Gunsteren, W. F.; DiNola, A.; Haak, J. R. Molecular Dynamics with Coupling to an External Bath. *J. Chem. Phys.* **1984**, *81*, 3684−3690.
(47) Udayabhaskararao, T.; Altantzis, T.; Houben, L.; Coronado-Puchau, M.; Langer, J.; Popovitz-Biro, R.; Liz-Marzán, L. M.; Vuković, L.; Král, P.; Bals, S.; Klajn, R. Tunable Porous Nanoallotropes Prepared by Post-Assembly Etching of Binary Nanoparticle Superlattices. *Science* **2017**, *358*, 514.
(48) Lee, H.-Y.; Shin, S. H. R.; Drews, A. M.; Chirsan, A. M.; Lewis, S. A.; Bishop, K. J. M. Self-Assembly of Nanoparticle Amphiphiles with Adaptive Surface Chemistry. *ACS Nano* **2014**, *8*, 9979−9987.
(49) Zeng, C. J.; Chen, Y. X.; Kirschbaum, K.; Lambright, K. J.; Jin, R. C. Emergence of Hierarchical Structural Complexities in Nanoparticles and Their Assembly. *Science* **2016**, *354*, 1580−1584.
(50) Yun, H.; Lee, Y. J.; Xu, M.; Lee, D. C.; Stein, G. E.; Kim, B. J. Softness- and Size-Dependent Packing Symmetries of Polymer-Grafted Nanoparticles. *ACS Nano* **2020**, *14*, 9644−9651.
(51) Reis, P. M.; Ingale, R. A.; Shattuck, M. D. Crystallization of a Quasi-Two-Dimensional Granular Fluid. *Phys. Rev. Lett.* **2006**, *96*, No. 258001.
(52) Zito, J.; Infante, I. The Future of Ligand Engineering in Colloidal Semiconductor Nanocrystals. *Acc. Chem. Res.* **2021**, *54*, 1555−1564.

https://doi.org/10.1021/acs.jpcb.2c07937
J. Phys. Chem. B 2023, 127, 2258−2266